JOURNAL OF GEOPHYSICAL RESEARCH, VOL. 105, NO. C2, PAGES 3497-3516, FEBRUARY 15, 2000

A semiparametric algorithm to retrieve ocean wave spectra from synthetic aperture radar

C. Mastenbroek and C.F. de Valk

Advisory and Research Group on Geo Observation Systems and Services, Vollenhove, Netherlands

Abstract. A new wave retrieval method for the ERS synthetic aperture radar(SAR) wave mode is presented. The new algorithm, named semiparametric retrieval algorithm (SPRA), uses the full nonlinear mapping relations as proposed by *Hasselmann and Hasselmann* [1991]. It differs from previous retrieval algorithms in that it does not require a priori information on the sea state. Instead, it combines the observed SAR spectrum with the collocated wind vector from the ERS scatterometer to make an estimate of the wind sea spectrum. The residual signal in the SAR spectrum is interpreted as swell. The method has been validated by collocating over 5 years of SAR wave mode observations with spectral buoy measurements at 11 locations on the open ocean. For wave components longer than 225 m, the standard deviation between the retrieved spectra and buoy observations is 0.41 m, which corresponds to a relative RMS error of 29%. About 10% of the observed SAR spectra were rejected, in particular in light wind conditions when nonwave features such as those caused by slicks dominated the imagette. The bias and scatter in the results obtained under light wind conditions could be reduced by introducing a wind-dependent tilt modulation. This wind-dependent tilt formulation is derived from the empirical CMOD4 relation between the wind vector, the incidence angle, and the radar backscatter for the ERS scatterometer.

1. Background

In this paper we present a method that extracts spectral wave data from ERS synthetic aperture radar (SAR) observations. The ERS-1 and ERS-2 satellites (launched in 1991 and 1995, respectively) have gathered a few million SAR spectra over the open ocean. The retrieval algorithm described here was developed to exploit this unique data set, and use it to augment the description of the wave climate in remote areas.

The way in which an ocean wave spectrum is mapped onto a SAR spectrum is reasonably well understood. *Hasselmann and Hasselmann* [1991], hereafter referred to as HH91, presented a closed set of equations, in which the SAR image spectrum is given as an expansion series in the ocean wave spectrum. The reason for the nonlinearity in this mapping is the fact that the orbital velocities of the waves interfere with the way in which the SAR constructs its resolution in the azimuth direction. The retrieval of an ocean wave spectrum from an observed SAR spectrum requires this nonlinear relation to be inverted.

HH91 presented an inversion method that changes a first guess wave spectrum iteratively until its associated SAR spectrum matches the observed SAR spectrum. The initial first guess wave spectrum is usually obtained from a numerical wave model. Modifications of this retrieval scheme have been applied in subsequent studies [*Brüning et al.*, 1994; *Hasselmann et al.*, 1996; *Heimbach et al.*, 1998]. *Krogstad et al.* [1994] developed a simplified approach that ignores the nonlinearities in the SAR mapping. This method was used by *Breivik et al.* [1998] to improve sea state forecasts.

The above mentioned retrieval algorithms are not optimally suited for the derivation of spectral wave climate data. First, both methods reject a sizable fraction of the observed SAR spectra: *Heimbach et al.* [1998] reported a rejection rate of 30%, *Breivik et al.* [1998] rejected half of the available SAR observations. It is clear that the rejection of such large portions of data has a detrimental effect on the wave climate statistics to be derived from the observations. Another limitation of both methods for our purpose is their dependence on the presence of a first guess wave spectrum from a wave model. To generate all wave spectra that are needed to compile a global wave atlas would require running a global wave model for the whole 8 year period since 1991.

The method described in this paper does not require a priori knowledge of the sea state to retrieve an ocean wave spectrum from a SAR observation. Instead, the fact that on the ERS satellites the scatterometer is operated simultaneously with the SAR wave mode is ex-

Paper number 1999JC900282.
0148-0227/00/1999JC900282$09.00

ploited. As the SAR measurement is located inside the scatterometer swath, each SAR wave mode spectrum can be associated with a wind vector from the scatterometer. Using a standard parameterization, a first guess wave spectrum is constructed. The stage of development and the exact propagation direction of the wind sea are found by minimizing the difference between the SAR spectrum calculated from the wind sea and the observed SAR spectrum. The residual signal in the observed SAR spectrum is interpreted as swell, and is translated from the SAR spectral domain into the wave spectral domain using a local linearization of the mapping relations.

To validate the retrieval method, 70 months of ERS-1/2 SAR wave mode observations have been collocated with spectral buoy measurements made at 11 locations (August 1992 to May 1998). An interesting conclusion of this study is that it is often possible to estimate the stage of development of the wind sea, even in cases where the longest wave component of the wind sea spectrum is located beyond the azimuth cutoff, so in the SAR spectrum no peak is visible at this location. *Kerbaol et al.* [1998] and others have estimated the cutoff wavelength from the correlation length in the azimuth direction. Given a wind speed, the stage of development of the wind sea can be estimated. In our method the wave age is determined by fitting the nonlinear mapping of a wind sea peak to the observed low azimuth wave number signal in the observed SAR spectrum. This fact, which has not been fully appreciated in the literature, is a consequence of the nonlinearity of the SAR mapping relations. Among other things, the nonlinearity causes a transfer of energy, from high to low azimuth wave numbers. Simulations have shown that wind sea spectra give rise to two symmetrical ridges on either side of the range axis in the SAR image spectrum [*Garello and Le Caillec*, 1997]. These structures are consistent with the conclusion of *Le Caillec et al.* [1996] that the interaction in the SAR spectrum is most effective between wave numbers that have the same projection on the azimuthal axis. Given the scatterometer wind speed, the stage of development of the wind waves can often estimated by matching the intensity of these structures in the SAR spectrum.

The most effective modulation mechanism in the case of spaceborne SARs is the orbital velocity bunching, in particular for waves propagating in the azimuth (or flight) direction. Waves propagating in the range direction are visible to the SAR only due to real aperture radar (RAR) modulation mechanisms. The most effective of these is the tilt modulation. In the standard formulation used by HH91 and many others, the tilt modulation is assumed to be wind independent. There are two reasons to believe that this is not the case in practice. The standard tilt formulation is based on the assumption that the slope in the wave spectrum at the Bragg wave number is independent of the wind. Observations do not support this assumption [*Apel*, 1994]. At low wind speeds these observations show an increase in the slope at the wave numbers that scatter C band waves, which would make the tilt modulation more effective under these conditions. This is consistent with the observations from the ERS-1/2 scatterometer. From observations with this instrument, that is also a C band radar, an empirical relation could be derived that expresses the radar backscatter as a function of the local wind vector [*Stoffelen and Anderson*, 1997]. Analysis of this relation, known as CMOD4, shows that it is consistent with a wave spectrum slope that increases with a decreasing wind.

In this study, CMOD4 has been used to reformulate the tilt modulation. This has resulted in a relation that is dependent both on the wind speed and on the angle between the wind direction and the radar look direction. Compared to validation results using the standard tilt relation, the wind-dependent tilt reduces the scatter for wave heights retrieved under low-wind conditions by more than 30%. For wind speeds over 10 m/s the improvement is much smaller (6%).

Finally, a preliminary comparison with results from the retrieval algorithm described in HH91 and subsequent papers is presented. It is found that occasionally SAR spectra are interpreted quite differently by both algorithms. A more comprehensive intercomparison, which involves collocating results from both models with in situ wave measurements, is recommended to analyze these differences.

2. Retrieval Method

The ocean wave spectrum is retrieved from the SAR spectrum in two distinct steps. In the first step the wind sea spectrum is estimated, combining wind information from the scatterometer with the SAR spectrum. In the second step the swell is determined from the residual SAR spectrum. In the following sections both steps in the retrieval process are discussed in detail.

2.1. Scaling of SAR Spectra

To produce calibrated radar images requires a considerable effort, as it involves the analysis of imagery over calibration sites to determine characteristics such as antenna patterns and power loss during acquisition. For the ERS SAR in image mode this has resulted in imagery with an absolute calibration within 0.4 dB [*Laur et al.*, 1996]. Though attempts have been made to calibrate the SAR wave mode results in a similar way [*Kerbaol et al.*, 1998], until now the SAR spectra that are reported have not been normalized with the mean cross section. Hence the SAR wave mode spectra have to be normalized in a different way. Following *Alpers and Hasselmann* [1982] we use the fact that the radar backscatter is related to the clutter noise level. This clutter noise level is derived from the SAR spectrum itself. The spectral distribution of the clutter noise is essentially white, so in practice it can be determined as the minimum value of the SAR power spectrum. For later use the procedure is presented more explicitly below.

The variance of the radar backscatter σ_0 in a single-look image is σ_0^2. In an n-look, intensity-averaged image the variance N_e decreases by a factor n. Amplitude averaging, which has been used for the ERS SAR wave mode data until June 1998, introduces an extra correction factor [*Brüning et al.*, 1994]. For a three-look, amplitude-averaged image this correction factor is $N_a/N_e = 0.78$. As the radar returns from within a single resolution cell are correlated, and the spectral shape of the clutter noise is assumed to be white, we have

$$\sigma_0^2 \int_{-k_a^N}^{k_a^N} \int_{-k_g^N}^{k_g^N} P_{cl} dk_g dk_a = N_a, \tag{1}$$

where P_{cl} is the clutter noise level, and $k_a^N = \pi/\rho_a$ and $k_g^N = \pi/\rho_g$ are the Nyquist wave numbers in the azimuth and range direction, respectively. They depend on the multilook azimuth resolution ρ_a and on the range resolution ρ_g. Integrating the above relation we get

$$P_{cl} = \frac{1}{(2\pi)^2} \frac{N_a}{N_e} \frac{\rho_g \rho_a}{n}. \tag{2}$$

As the multilook azimuth resolution is n times the single-look resolution ρ_{sl}, the clutter noise level P_{cl} is independent of the number of looks that is chosen in the SAR processing. If we are now presented with a spectrum $Q(\mathbf{k})$ of a three-look, amplitude-averaged SAR image with a clutter noise level equal to Q_{cl}, it can be calibrated using the following equation:

$$P_{obs}(\mathbf{k}) = \frac{0.78}{(2\pi)^2} \frac{\rho_a \rho_g}{3} \frac{Q(\mathbf{k})}{Q_{cl}}. \tag{3}$$

The calibrated SAR spectrum $P_{obs}(\mathbf{k})$ has now a clutter noise level equal to P_{cl} in (2).

The ERS SAR wave mode product is provided by the European Space Agency (ESA) on a 12 by 12 polar grid, with an angular discretization of 15°, and with the wavelength increasing logarithmically from 100 m to 1000 m. Following *Hasselmann et al.* [1996] the clutter noise level Q_{cl} is calculated as the mean spectral level of the five lowest directional bins at the shortest wavelength.

Hasselmann et al. [1996] assumed the size of the spatial resolution cell ρ_g, ρ_a to be 30 by 30 m, which coincides to a certain extent with the nominal resolution specified by ESA of 25 by 22 m. In this study the resolution cell was assumed to be 33 by 33 m.

2.2. Nonlinear Relation Between Wave Spectra and SAR image spectra

A SAR uses the Doppler shift in the returned radar signal to determine the position of the scatterer in the azimuthal direction. When a target is moving toward the radar, the additional Doppler shift causes it to be displaced in the positive azimuthal direction in the SAR image plane. Owing to their orbital velocities, ocean waves represent a collection of moving targets. This has a profound effect on the mapping of an ocean wave spectrum onto a SAR image spectrum. For waves with a component in the azimuth direction, the Doppler shifts caused by their orbital velocities act as an additional modulation mechanism: the so-called velocity bunching effect. However, the RMS of the azimuthal displacements induced by the orbital velocities of all wave components taken together causes a degradation of the azimuthal resolution. Wave components beyond a certain azimuthal cutoff wave number are not mapped onto the SAR image directly. The nonlinearities in the mapping mechanism cause their energy to be transfered to low azimuthal wave numbers [e.g., *Hasselmann et al.*, 1985].

To gain insight into the role of, in particular, the nonlinearity of the mapping relations we will analyze the example presented in Figure 1. The upper left panel shows the ocean wave spectrum. It consists of a fully developed wind sea associated with 12 m/s wind blowing in the positive azimuth direction, and of a 300 m long swell traveling in the range direction (the wind sea is simulated with a JONSWAP-type parameterization proposed by *Donelan et al.* [1985], the swell is Gauss-shaped with a spectral width of 4.2×10^{-3} rad/m). The upper right panel shows the SAR image spectrum using the so-called quasi-linear approximation to the mapping relations (HH91). In this approximation the azimuth cutoff is included, which explains why the wind sea peak has disappeared. However, in the quasi-linear approach the transfer of energy is neglected. This becomes apparent when we look at the SAR image spectrum calculated with the full nonlinear transform (bottom left panel in Figure 1). Compared to the SAR spectrum calculated with the quasi-linear model it shows two distinct ridges parallel to the range axis. The bottom left panel shows the effect of the nonlinearity of the mapping relations. The distinct spectral shape of the nonlinear ridges has also been found by *Garello and Le Caillec* [1997], where they were identified as the result of quadratic interactions. In the semiparametric retrieval algorithm (SPRA) presented below, these ridges in the SAR spectrum are combined with wind vector information from the scatterometer to estimate the stage of development of the wind sea.

In the retrieval algorithms published to date, the nonlinearity of the mapping relations has been simplified. *Krogstad et al.* [1994] used an optimized quasi-linear transformation, in which the nonlinear effects are believed only to counteract the azimuthal smearing. In the retrieval algorithm described in HH91 and subsequent papers, differences between the calculated and the observed SAR spectra are mapped back to the wave spectrum using the quasi-linear model. Hence mismatches in the low azimuth wave number part of the SAR spec-

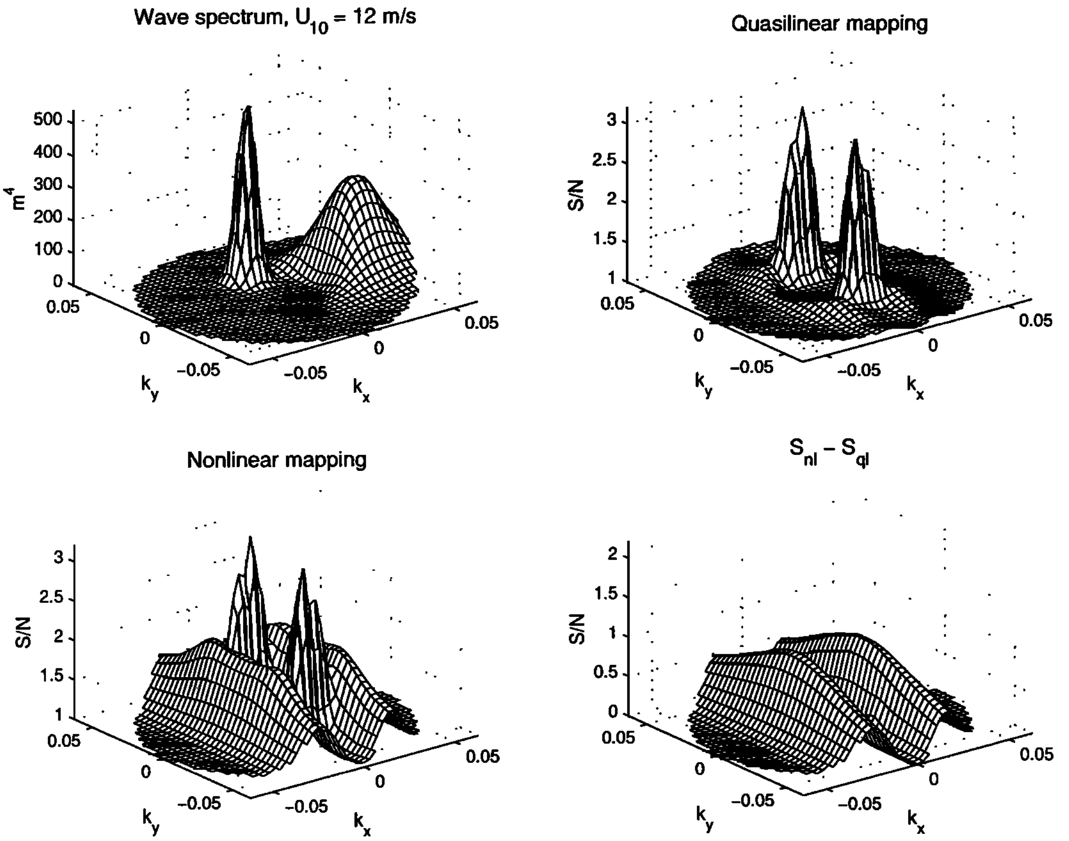

Figure 1. Quasi-linear and nonlinear synthetic aperture radar (SAR) image spectrum of an ocean wave spectrum consisting of a wind sea and a swell peak.

trum due to an inadequate wind sea spectrum tend to be attributed to swell peaks.

2.3. Modulation Transfer Functions

In this study we use the closed nonlinear transformation that relates the wave spectrum $F(\mathbf{k})$ to the SAR image spectrum $P(\mathbf{k}) = \Phi(F(\mathbf{k}))$ as originally proposed by HH91. An alternative derivation of these relations is presented by *Krogstad* [1992]. Compared to the relations as formulated by HH91, several modifications have been made. First the range-bunching mechanism is included [c.f., *Engen and Johnsen*, 1995]. For high sea states the range bunching has a noticeable effect on the simulated SAR spectra, but overall its significance is limited.

More important are the changes in the tilt modulation. HH91 used a standard formulation for the tilt modulation, that can be derived as follows. Assuming Bragg scattering is dominant, the radar backscatter σ_0 is proportional to a polarization-dependent, geometric scattering function G_{VV} and the spectral level $S(k_B)$ at the Bragg wave number k_B:

$$\sigma_0 = 16k_r^4 G_{VV}\left(S(\mathbf{k_B}) + S(-\mathbf{k_B})\right), \qquad (4)$$

where the Bragg wave number is related to the wave number of the radar: $k_B = 2k_r \sin\theta$. The dimensionless modulation transfer function caused by a tilting surface is defined by

$$T_t = \frac{1}{\sigma_0}\frac{\partial\sigma_0}{\partial\theta}\frac{k_{\text{look}}}{k}. \qquad (5)$$

The geometric scattering function G_{VV} can be approximated by $(1+\sin^2\theta)^2$. Assuming the wave number spectrum $S(k)$ is proportional to k^{-4} in the vicinity of the Bragg wave number k_B, this leads to the expression of the tilt modulation used by HH91:

$$T_t = -\frac{4i}{\tan\theta}\left(\frac{1}{1+\sin^2\theta}\right)\frac{k_y}{k}. \qquad (6)$$

As mentioned above, there are two indications that the tilt modulation may actually be wind dependent. Measurements on short waves indicate that their spectral energy may decay faster than k^{-4} for lower wind speeds [cf. *Apel*, 1994]. This is consistent with the wind speed dependence of the radar backscatter observed with the ERS-1/2 scatterometer. Like the ERS-1/2 SAR, the scatterometer is a C band, VV-polarized radar. *Stoffelen and Anderson* [1997] have parameterized the radar backscatter measured by the scatterometer in terms of the incidence angle, the wind speed U_{10} and the angle ϕ between the radar look direction and the wind: $\sigma_0 = \sigma_0(\theta, U_{10}, \phi)$. When we insert this parameterization, known as CMOD4, in equation (5) we obtain

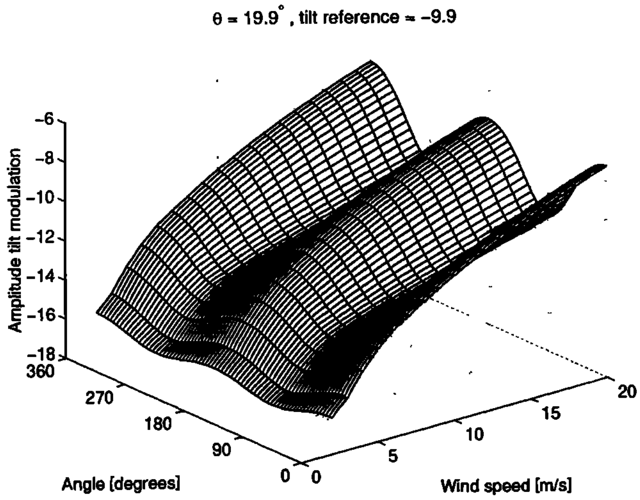

Figure 2. Amplitude of the tilt modulation as a function of wind speed and the angle between the radar look direction and the wind direction. Compared to the standard formulation, the wind-dependent tilt modulation derived from the CMOD4 relation becomes more effective for low wind speeds.

a wind-dependent relation for the tilt modulation. In principle, the differentiation in (5) could be performed analytically. However, due to the complicated functional form of CMOD4, it has proven to be more practical to determine the derivative numerically.

Figure 2 shows the tilt modulation caused by a range-traveling long wave (the last condition ensures that $k_y/k = 1$) as a function of wind speed and wind direction. The incidence angle is assumed to be 19.9°; the wind direction is defined relative to the look direction of the radar. According to the standard tilt relation (6), the amplitude of the tilt modulation has a constant value of 9.9 for this incidence angle. From Figure 2 we see that this value corresponds roughly to the values derived from CMOD4 for wind speeds over 10 m/s. For lower wind speeds the tilt modulation derived from the CMOD4 parameterization is more effective. Assuming Bragg scattering, this corresponds to a larger slope in the wave number spectrum for these waves, which is in qualitative agreement with the results reported by *Apel* [1994]. For a 2 m/s wind speed the tilt modulation derived from CMOD4 is 60% larger than the standard value given by (6).

A second feature that is apparent from Figure 2 is the dependence of the tilt modulation on the wind direction, in particular for wind speeds over 10 m/s. The Figure indicates that for these wind speeds the tilt modulation is 20 to 30% more effective when the look direction and the wind make an angle of 90°, compared to the case when these two are aligned. This indicates that the spectral slope in the vicinity of the Bragg waves is not isotropic.

The validation presented below will show that the incorporation of the tilt modulation derived from the CMOD4 relation results in a significant reduction of the scatter in the retrieved wave height, in particular under light wind conditions. Further progress along these lines may very well be possible. Measurements indicate that both the phase and the amplitude of the hydrodynamical modulation may be wind speed dependent [*Keller and Wright*, 1975]. Inclusion of this effect may result in a further improvement in the understanding of SAR imaging of ocean waves.

2.4. General Description of the SPRA Retrieval Method

The retrieval of a wave spectrum with the SPRA algorithm takes place in two steps. In the first step, the wind vector from the scatterometer is used to construct a wind sea spectrum. For this purpose the parameterization of *Donelan et al.* [1985] is used. Unlike the case with the JONSWAP spectrum [*Hasselmann et al.*, 1973], the level of the spectral tail in the spectrum of *Donelan et al.* is wind speed dependent. This gives better agreement with spectra observed by buoys. The stage of development of the wind sea and its mean propagation direction will be found from minimizing the difference between the simulated and the observed SAR spectrum. As a first guess, we assume that the wind sea is fully developed and that the waves are propagating in the wind direction.

Subsequently the SAR spectrum associated with this estimated wind sea spectrum is calculated using the nonlinear mapping relations from HH91: $P_{ws}(\mathbf{k}) = \Phi(F_{ws})(\mathbf{k})$. This simulated SAR spectrum is then compared with the observed SAR spectrum P_{obs}. The difference between the observed and simulated SAR spectrum is expressed in terms of a cost function, where the functional form of this cost function is derived from the statistics obeyed by an observed SAR spectrum (see Appendix A). This cost function is then minimized with respect to the two free parameters in the wind sea parameterization: the stage of development and the mean propagation direction.

After the optimal set of wind sea parameters has been found, the residual signal in the observed SAR spectrum is interpreted as resulting from waves that are not part of the parametric wind sea spectrum, that is, swell. Given the wind sea spectrum, wave components longer than the wind sea peak are generally mapped linearly by the SAR (see discussion below). So when we write the SAR mapping as a Taylor expansion around $F = F_{ws}$ we can neglect quadratic and higher-order terms:

$$P(\mathbf{k}) \simeq \Phi(F_{ws})(\mathbf{k}) + \left.\frac{\partial \Phi(F)(\mathbf{k})}{\partial F(\mathbf{k}')}\right|_{F=F_{ws}} F_{swell}(\mathbf{k}'), \quad (7)$$

where F_{swell} is the spectrum of the swell waves. As the linear SAR mapping is local in the wave number space, we can define a gain function $\alpha(\mathbf{k})$ that maps the swell spectrum to the SAR spectrum:

$$\alpha(\mathbf{k})\delta_{\mathbf{kk}'} = \left.\frac{\partial\Phi(F)(\mathbf{k})}{\partial F(\mathbf{k}')}\right|_{F=F_{ws}}. \quad (8)$$

Note that $\alpha(\mathbf{k})\delta_{\mathbf{kk}'}$ is an approximation of the tangent linear model of Φ at the wind sea spectrum F_{ws}, valid in the wave number range where the SAR mapping is approximately linear.

Given an observed SAR spectrum $P_{obs}(\mathbf{k})$ with clutter noise level P_{cl}, and the estimate of the contribution of the wind sea to the SAR image spectrum, equation (7) can be solved for the swell spectrum $F_{swell}(\mathbf{k})$ using $\alpha(\mathbf{k})$ from equation (8):

$$F_{swell}(\mathbf{k}) = \frac{P_{obs}(\mathbf{k}) - P_{cl} - P_{ws}(\mathbf{k})}{\alpha(\mathbf{k})}. \quad (9)$$

The gain function for the swell $\alpha(\mathbf{k})$ is calculated numerically by perturbing the estimated wind sea spectrum F_{ws} and comparing its nonlinear SAR mapping with that of the unperturbed wind sea spectrum. The above procedure will only retrieve the swell spectrum in the part of the wave number domain that is accessible to the SAR. In the present case that means that the swell has to be longer than about 100 m, and that its azimuthal wave number has to be smaller than the cutoff wave number.

It is important to distinguish between the tangent linear approximation for the swell presented above, and the quasi-linear approximation described in HH91. The tangent linear model is superior to the quasi-linear model, as the latter ignores all nonlinear contributions except those that cause the azimuthal smearing. Figure 1 illustrates this difference. In the procedure outlined above, the observed low azimuth wave number ridges caused by the energy transfer from higher wave numbers is attributed to the wind sea. Using the tangent linear model, only the signal in excess of these ridges in the observed SAR spectrum is assumed to be the result of (linearly mapped) swell. If a quasi-linear model would is to retrieve the swell, the low azimuth wave number ridges caused by the nonlinear transfer of energy would also be attributed to swell, as this model does not include the high-to-low azimuth wave number energy transfer. Neglecting the nonlinear interactions, the quasi-linear model also underestimates the azimuth cutoff wave number. As the tangent linear model is an expansion around the part of the spectrum that is responsible for the bulk of the nonlinearity, it includes most of the modification of the cutoff due to the nonlinearity.

We will now address the question why the wave components longer than the wind sea peak are generally mapped linearly by the SAR. The nonlinearity of the SAR mapping is caused by the fact that the ocean surface is moving, that is, by the orbital velocity of the waves. Swell waves longer than 100 m contribute only marginally to the total orbital velocity variance. It follows that the mapping of the wind sea is not significantly affected by the presence of these longer waves. This is the reason that we can estimate the wind sea parameters without any information concerning the presence of swell. Once these wind sea parameters and the associated orbital velocity variance are found, the so-called azimuthal cutoff wave number can be calculated. From the integral relation in HH91 it follows that wave components with an azimuthal wave number much smaller than this cutoff are mapped linearly by the SAR. In nature the orbital velocity variance and the peak wave number of a pure wind sea spectrum are related, much in the same way that the energy and the peak are related. In Appendix B this empirical notion is used to derive a tentative relation between the cutoff wave number and the location of the wind sea peak. It follows that in the spectral domain of the present ERS SAR wave mode product, which ranges from 100 to 1000 m, wave components longer than the peak are mapped linearly.

Note that by using the above scheme, the swell spectrum $F_{swell}(\mathbf{k})$ will have a 180° ambiguity in its propagation direction. The present ERS-1/2 SAR user wave (UWA) product only provides a power spectrum of the SAR image. Hence all the directional information it contains is the alignment of the wave crest, not the direction in which these crests are moving. In the future, using the advanced synthetic aperture radar (ASAR) carried by ENVISAT, the 180° ambiguity may be resolved, as the ASAR wave mode product will be based on cross spectra of two looks separated in time. For the present we have decided to accept the 180° ambiguity of the ERS data and develop our scheme for this product, as it gives access to over 7 years of spectral wave measurements with a global coverage.

2.5. Implementation of the Retrieval Method

The SPRA retrieval method has been applied to archived ERS-1/2 SAR wave mode observations. In the previous section an overview of the algorithm was presented, and the main assumptions were discussed. Here we will give a more detailed account of the different stages in the processing of the satellite data.

1. The ERS-1/2 SAR wave mode product is provided on a 12 by 12 wavelength/direction grid. The wavelengths range from 100 to 1000 m, the direction spans 180° in 15° increments. To facilitate their interpretation these spectra are collocated with scatterometer wind vectors. In the collocation a maximum distance of 50 km is allowed between the two measurements, which corresponds to the spatial resolution of the scatterometer.

2. Before being interpolated to a square wave number grid, the SAR spectra are normalized using their clutter noise level and filtered. The normalization is discussed above in section 2.1. The filtering is essential to eliminate contributions caused by nonwave features such as slicks. It was found that nonwave contributions can be effectively removed by evaluating the SAR spec-

Table 1. Overview of the ERS SAR Wave Mode Data Available for the Present Study

From	Until	Satellite	Incidence Angle
Sept. 1991	April 1995	ERS-1	19.9°
May 1995	April 1996	ERS-1	23.0°
May 1996	May 1998	ERS-2	23.0°

trum averaged over the propagation angle. The filtering exploits the fact that the spatial scales of slicks are usually larger than the length of the longest swell waves. In a typical slick-dominated SAR spectrum the spectral level is monotonically increasing with wavelength. Hence the filtering routine rejects all wavelength bins involved in such behavior. Below in section 3.6 the merits of this filtering technique are evaluated using buoy data. The computations were performed on a 64 by 64 wave number grid, using a grid spacing of $\Delta k = 3.3 \times 10^{-3}$ rad/m.

3. A first guess wind sea spectrum is constructed using the scatterometer wind measurement and the spectral shape proposed by *Donelan et al.* [1985]. For wind speeds below 10 m/s the wind sea is assumed to be fully developed ($U_{10}/c_p = 0.9$, where U_{10} is the wind speed at 10 m height and c_p the phase velocity of the spectral peak) and aligned with the wind direction. For wind speeds above 10 m/s the wave age U_{10}/c_p is increased in steps of 0.1 until the cost function no longer decreases. Subsequently, the cost function is minimized with respect to the propagation direction.

4. From the residual SAR image spectrum, that is, the observed SAR spectrum minus the clutter noise minus the estimated wind sea contribution, the ocean swell spectrum is estimated (see section 2.4). Unlike the estimate of the wind sea spectrum, the estimate of the swell spectrum is completely nonparametric. The estimate of the swell spectrum is only retained if its inclusion decreases the cost.

5. Given the swell estimate, the wind sea spectrum parameters are estimated once again. Occasionally, the contribution of the swell to the cutoff results in a reduction of the most likely wave age of the wind sea.

6. Finally, the swell spectrum is computed again, now using the updated estimate of the wind sea peak. The orbital velocity variance of the swell peak from the first iteration is taken into account in the derivation of the tangent linear model that is used to interpret the residual SAR spectrum.

3. Validation of the Retrieved Wave Spectra Using NOAA Buoys

3.1. Observations From the ERS-1/2

Barring the few minutes per orbit that it is switched in image mode, the SAR on board the ERS satellites acquires two wave mode spectra per minute, which puts these spectra 200 km apart. As of the middle of 1998, this has resulted in a data set of more than 4 million SAR spectra acquired over open sea. This amounts to roughly 1000 observations in each cell of 3° longitude by 3° latitude. The incidence angle at which these spectra are acquired is kept mostly constant in time (see

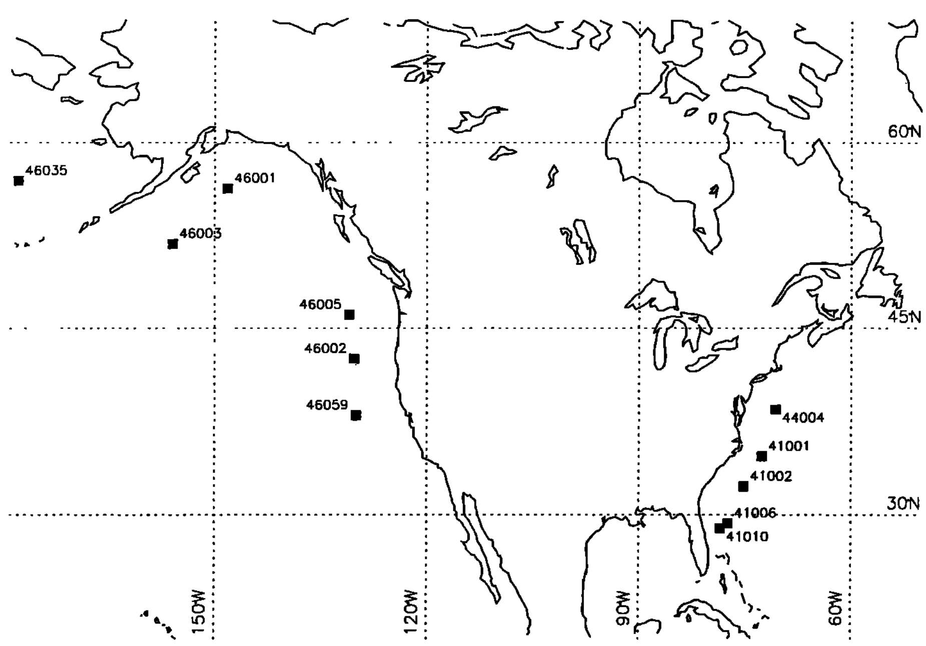

Figure 3. Location of the 11 spectral NOAA buoys used for the validation of the SAR wave mode retrieval algorithm.

Table 1). In the first 4 years of the operation of the ERS-1 (September 1991 until April 1995) it was set at 19.9°, which is the steepest angle allowed by the instrument. Starting from May 1995 the incidence angle was set at 23.0°, a value that was maintained after the ERS-2 took over in May 1996.

Interleaved with the SAR wave mode, the Active Microwave Instrument (AMI) of the ERS satellites operates the scatterometer. As the swath of the SAR is entirely covered by that of the scatterometer, each SAR wave mode spectrum can be collocated with a wind vector derived from the scatterometer. For this study the scatterometer winds were obtained from the wind field (WNF) product that is distributed by the Centre ERS d'Archivage et de Traitement (CERSAT). Comparison of the WNF wind speed with buoy measurements has shown that the standard deviation is below 2 m/s, with a negligible bias [*Quilfen and Bentamy*, 1995].

3.2. Selected Buoys

To validate the ocean wave spectra retrieved from SAR observations, they have been compared with spectral buoy measurements. The most important data set to do this is provided by the National Oceanic and Atmospheric Administration (NOAA) buoy network. NOAA operates 50+ buoys, located mainly in American coastal waters, that report the one-dimensional energy density wave spectrum every hour. For the comparison with the satellite-retrieved data, 11 buoys were selected that were operational since 1992 and that are located at least 100 km offshore (see Figure 3). The latter condition was imposed to avoid problems with the representativeness of the buoy observation for its immediate surroundings. There is ample literature on the accuracy of the energy density spectra recorded by buoys [cf. *Long*, 1980]. In general it can be said that the accuracy in the significant wave height is of the order of 5-10%, depending on the peak period and spectral width of the waves.

The spectral buoy data itself were obtained from two different sources. The first three years of data (September 1992 to December 1995) were taken from the F291 CD-ROMS provided by the National Oceanographic Data Center (NODC). The spectral buoy data recorded after 1995 were obtained from the web site of the National Buoy Data Center (NBDC). Before being used in the intercomparison, the consistency of the data was checked. This involved eliminating observations that were reported more than once, and comparing significant wave height values reported with those computed from the energy density spectrum. The wind speed was converted from measurement height (usually 5 m) to a reference height of 10 m assuming a logarithmic wind profile and a standard drag relation. Finally, the data records were given a new time tag. In the original data set the acquisition time is reported in whole hours, where it is understood that the actual wave measurement took place between 30 and 10 min before this time. The new time tag, which is used in the collocation with the satellite data, puts the acquisition time in the middle of this 20 min integration time.

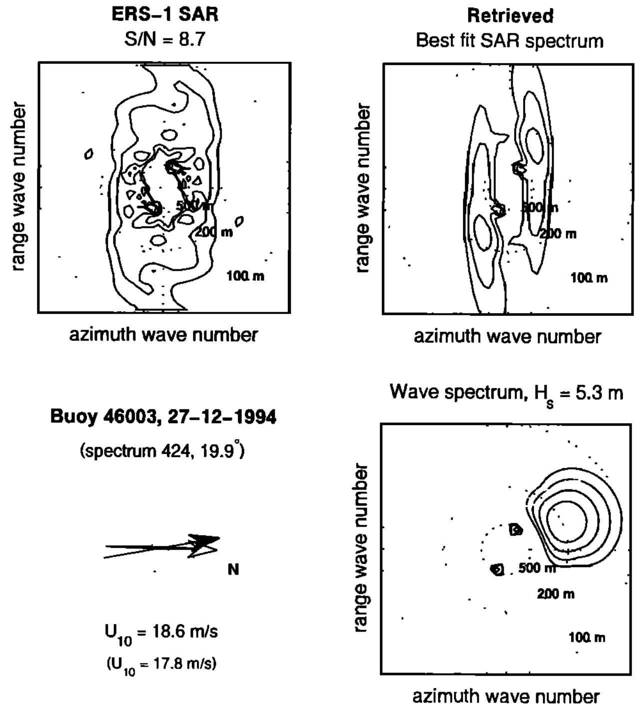

Figure 4. Spectra observed near buoy 46003 at December 27, 1994, 0826 UT: (top left) SAR spectrum observed by the ERS-1; (top right) simulated SAR spectrum; (bottom right) wave spectrum retrieved with the semiparametric retrieval algorithm (SPRA). A contour line in the spectrum corresponds to a change in the spectral level of 2 dB, which is equivalent to a factor of 1.6. (bottom left) The arrow with the solid tip indicates the scatterometer wind vector, and the open tip arrow corresponds to the buoy wind. The wind speed in parentheses refers to the buoy measurement.

Ocean wave spectra retrieved from ERS SAR wave mode observations were collocated with buoy records for the period of September 1992 until May 1998. The maximum distance allowed between the SAR observation and the buoy location was set at 60 km, the maximum temporal interval at 30 min. In this way a total of 595 SAR wave mode spectra could be collocated with a valid buoy measurement. Of these 595 cases, 58 (i.e., 10%) could not be interpreted by the retrieval algorithm as the SAR spectrum was considered to be too contaminated by nonwave features by the filtering routine.

3.3. Examples of Retrieved Spectra

In section 2.2 it was shown that the nonlinearity in the SAR mapping relations can cause a transfer of energy from large to small azimuthal wave numbers, thus providing information on waves that are otherwise invisible to the SAR. A case in point is shown in Figures 4 to 6. The SAR spectrum acquired by the ERS-1 near buoy 46003 on December 27, 1994 (Figure 4, up-

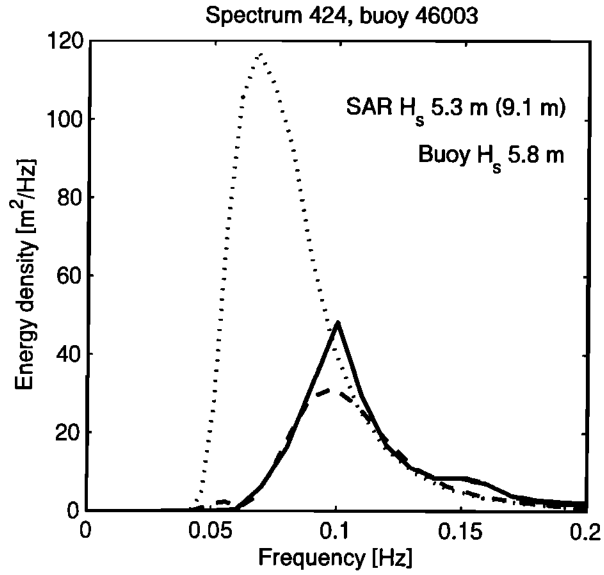

Figure 5. Energy density spectra for the case shown in the previous figure: solid line, buoy observation; dashed line, wave spectrum derived from SAR; dotted line, wave spectrum assuming a fully developed wind sea.

per left panel) shows very little structure, except that the energy tends to be aligned with the range axis. The signal-to-noise ratio of the peak in the SAR spectrum is 8.7. Both the scatterometer and the buoy indicate

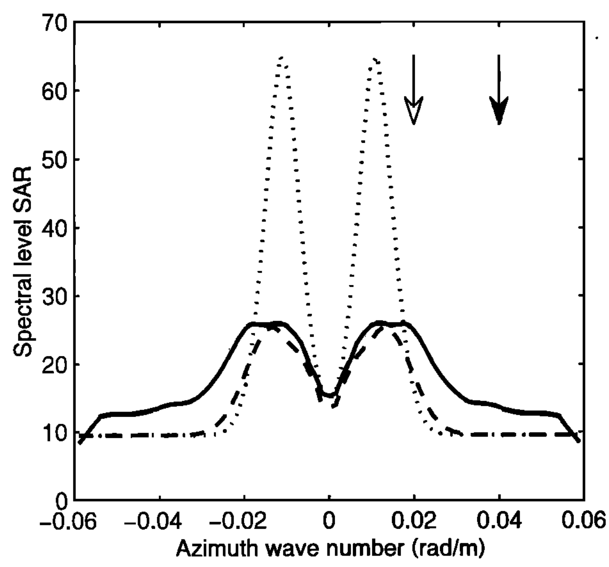

Figure 6. Observed and simulated SAR spectra averaged over the range wave number axis. When a fully developed wind sea is assumed (dotted line), the low azimuth wave number ridges caused by the nonlinear transfer from higher azimuth wave numbers are significantly larger than the signal observed by the SAR (solid line). When these low azimuth wave number ridges are used to determine the stage of development, a much better fit can be obtained (dashed line). The arrows indicate the locations of the peak of the fully developed wind sea (open tip), and of that of the wave spectrum derived from the SAR (solid tip).

that a strong wind of 18 m/s is blowing in the positive azimuth direction. The buoy measurement (Figure 5, solid line) shows a single-peaked spectrum with its spectral peak at 0.1 Hz, which corresponds to a wavelength of 150 m in deep water. With a wave age $U_{10}/c_p = 1.15$, this makes it an underdeveloped wind sea. As in the example shown in Figure 1, the azimuth-traveling wind sea is beyond the azimuthal cutoff.

However, even though the peak itself is not visible in the SAR spectrum, the nonlinearity in the SAR mapping induces an energy transfer from high to low azimuth wave numbers. The spectral shape of this low azimuth wave number signal, two ridges parallel to the range axis, can be clearly observed in the SAR spectrum in Figure 4. The level of these low azimuth wave number ridges is related to the level of the wind sea spectrum. It follows that by matching the low azimuth wave number signal produced by the nonlinear mapping of the wind sea peak, the retrieval algorithm is able to estimate the stage of development of the wind sea. This is illustrated in Figure 6. Here the simulated and observed SAR spectra are shown averaged over the range axis. The dotted line corresponds to the SAR signal produced by a fully developed wind sea. The Figure clearly shows that in that case the level of the low azimuth wave number signal would be much higher than the observed signal (full line). When the scheme is allowed to fit the observed level of the low azimuth wave number signal, a wave age of $U_{10}/c_p = 1.2$ is found (dashed lines in the Figures 5 and 6). Obviously the shape of the buoy spectrum does not exactly match that of the *Donelan et al.*

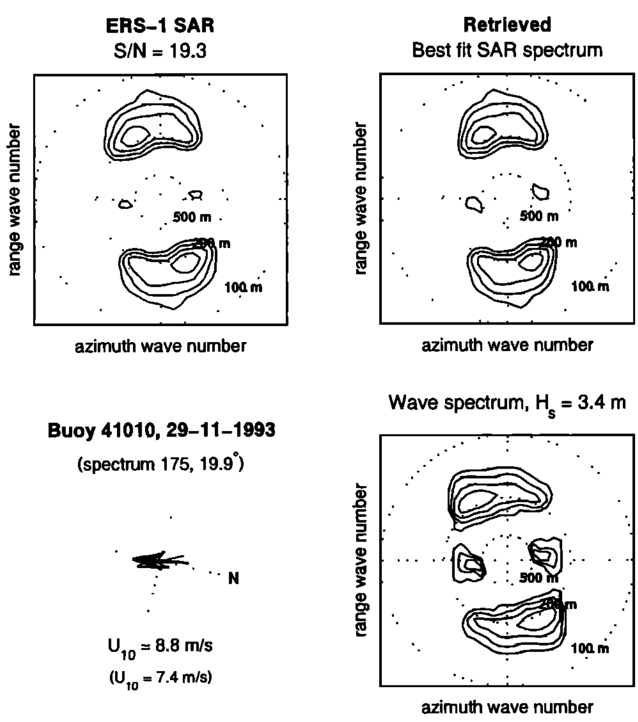

Figure 7. Observed (solid line) and retrieved (dashed line) spectra near buoy 41010 on November 29, 1993, 0336 UT.

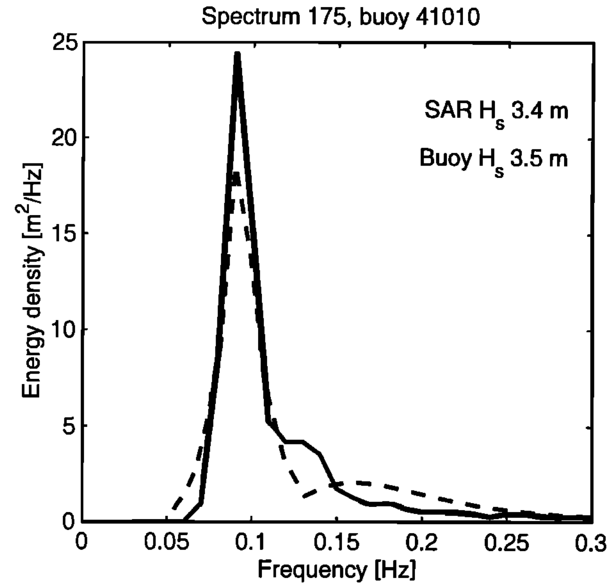

Figure 8. Comparison of the energy density spectra near buoy 41010 corresponding to the case in the figure 7. Solid line denotes buoy observation; dashed line denotes wave spectrum derived from SAR..

[1985] parameterization, which explains the difference in significant wave height of 0.5 m.

Note that in the above case an estimate of the stage of development of a wind sea could be made, despite the fact that the azimuth resolution of the SAR was degraded so much that the wind waves could not be observed in the SAR spectrum. However, the transfer of energy from high to low azimuth wave numbers induced by the nonlinearities in the SAR mapping results in noise-like ridges in the SAR spectrum. By matching the height of these ridges, the stage of development can be estimated.

In the example discussed above, the whole signal could be explained as emanating from a single wind sea peak. In the example shown in Figures 7 and 8 the opposite is the case. Here the observed SAR spectrum shows a peak at a wavelength just short of 225 m almost in the range direction. Given the wind of 8 m/s in the negative azimuth direction, this signal must correspond to a swell system. Indeed, the buoy observed a peak at 0.09 Hz, which corresponds to a wavelength of just under 225 m. The retrieval algorithm is able to reproduce the peak frequency of the swell system quite accurately; the energy in the swell system is underestimated slightly. Note that in the two-dimensional ocean wave spectrum shown in Figure 7, lower right, the energy of the swell system is divided over two symmetrical peaks. This reflects the 180° ambiguity in the retrieved swell propagation direction.

3.4. Validation of the Retrieved Wave Height and Period

Given its resolution of about 30 m, the ERS-1/2 SAR can only resolve waves longer than 100 m, which corresponds to waves with periods longer than 8 s in deep water. In high seas the resolution in the azimuth direction may be even lower due to smearing. Information on shorter wave components is derived indirectly by combining the scatterometer wind with the level of low azimuth wave number ridges in the SAR spectrum. Though the level of these shorter wave components influences the mapping of the longer wave components, and is therefore important in the retrieval process, the true strength of the SAR lies in its ability to detect the height and direction of the longer wave components. To enable a statistical analysis of the performance of the SAR, we use the following measure of the wave height in the frequency interval $[f_1, f_2]$:

$$H = 4\left(\int_{f_1}^{f_2} F(f)df\right)^{1/2}, \tag{10}$$

with $F(f)$ the elevation spectrum in terms of frequency.

To validate the SPRA algorithm, we first concentrate on the wave components resolved by the SAR. In Fig-

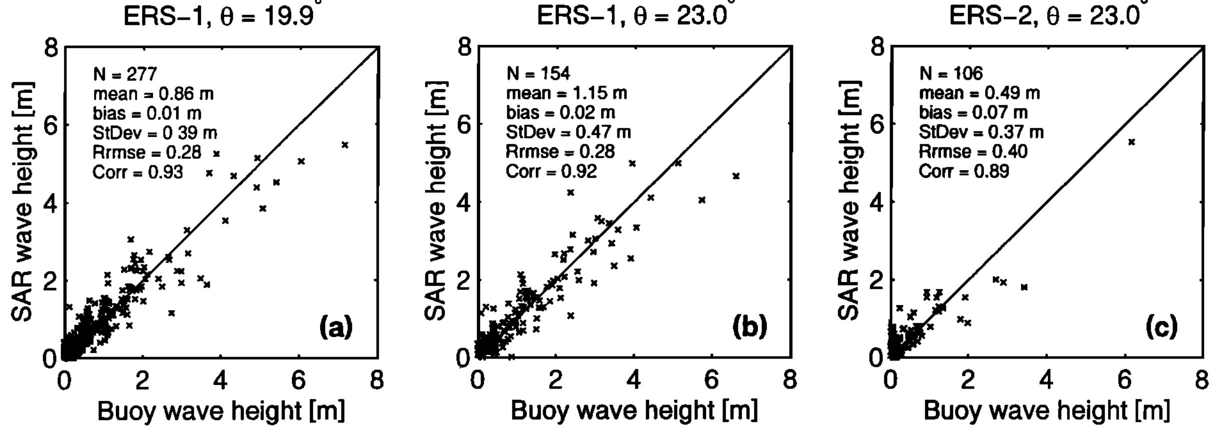

Figure 9. Retrieval of the height of the wave components longer than 12 s (225 m): (a) ERS-1 with incidence angle of 19.9°; (b) ERS-1, 23.0°; (c) ERS-2, 23.0°.

Table 2. Validation of the Height of Wave Components With a Period Longer Than 12 s, Using Four Different Maximum Distances in the Collocation of Buoy Data and SAR Wave Mode Observations.

	< 50 km	< 60 km	< 100 km	< 200 km	< 300 km
N	363	537	1414	5486	12265
Mean, m	0.84	0.87	0.91	0.94	0.95
Bias, m	0.02	0.03	0.03	0.02	0.01
s.d., m	0.40	0.41	0.47	0.50	0.55
RRMSE	0.29	0.29	0.33	0.35	0.38

Here, s.d. denotes standard deviation. The relative RMS error (RRMSE) is defined as the RMS error normalized with the RMS buoy wave height. The maximum temporal interval was 30 min in all cases.

ure 9 the retrieved height of the wave components longer than 12 s is plotted against buoy observations. This height is calculated from the one-dimensional energy density spectra with equation (10), inserting $f_1 = 0$ and $f_2 = 1/12$ Hz. In the main part of the validation we concentrate on the wave components with periods longer than 12 s, which correspond to wavelengths longer than 225 m in deep water, because these waves fall well into the spectral range resolved by the SAR, and are generally not subject to suppression due to azimuthal smearing. In Figure 9, results are presented for the three acquisition periods of ERS-1/2 (see also Table 1). The change in incidence angle during the ERS-1 mission apparently had an adverse effect on the standard deviation, which increased from 0.39 m to 0.47 m. However, this can be attributed largely to the increase in the average wave height from 0.86 m to 1.15 m: The relative RMS error (RRMSE), defined as the RMS error normalized with the RMS wave height observed by the buoy, remained constant at 28%.

In the collocation of buoy and SAR wave mode observations the maximum distance between the two was set at 60 km. The maximum time difference was fixed at 30 min, but as the NOAA buoys report observations every hour, no significant amount of data was rejected by this criterion. The influence of the maximum distance that is allowed can be assessed with the data presented in Table 2. In that table, validation results are presented for five different maximum collocation distances. We find that the scatter increases significantly when the spatial collocation criterion is relaxed: The relative RMS error increases from 29% when the distance between buoy and SAR is 50 km or less, to 55% when this distance is allowed to be 300 km.

Despite the fact that for ERS-2 a data set of 25 months was available (ERS-1 operated only 11 months with an incidence of 23°, for instance), only a limited number of collocations could be made for ERS-2. This is caused by the fact that the acquisition pattern of SAR wave mode data of ERS-2 is different from that used for ERS-1. For technical reasons, no SAR wave mode observations are made in several regions adjacent to the coast. Unfortunately, one of these is an area several hundred kilometers wide along the west coast of North America, an area that includes most of the NOAA buoys in the Pacific used in this study. This explains also the low average height of waves longer than 12 s observed by ERS-2. The NOAA buoys in the northeast Pacific are exposed to more swell than the buoys in the northwest Atlantic. This change in acquisition pattern makes it very difficult to assess the performance of the ERS-2 SAR wave mode, and to compare it with that of ERS-1.

In Figure 10 the performance of the SPRA retrievals is assessed per frequency interval. As before, the height of the waves in each frequency interval is calculated from the one-dimensional spectrum with (10), using different integration boundaries for each frequency interval. The energy in the shortest wave components, with wave periods between 8 and 12 s, is underestimated. This may be caused by the azimuth cutoff, which obviously has its largest effect on the shortest wave components. The performance of the system is optimal for waves with periods between 12 and 15 s. The relative RMS error in the retrieval of the height of these waves is 31%; the standard deviation is 0.38 m. For waves with periods longer than 15 s the standard deviation is even smaller, 0.28 m, but given the limited amount of energy in this frequency band, the relative performance is worse (35%).

The SPRA algorithm combines the measurements of the SAR and the wind scatterometer to retrieve the ocean wave spectrum. Obviously, the wind speed and sea state are related. Hence we may wonder how much information on the sea state comes from the scatterometer data, and how much is gained by including the SAR image spectrum in the analysis. Without information on the presence of swell or on the stage of development of the wind sea, the rule-of-thumb estimate of the significant wave height at open sea is

$$H_s = 0.24\frac{U_{10}^2}{g}, \tag{11}$$

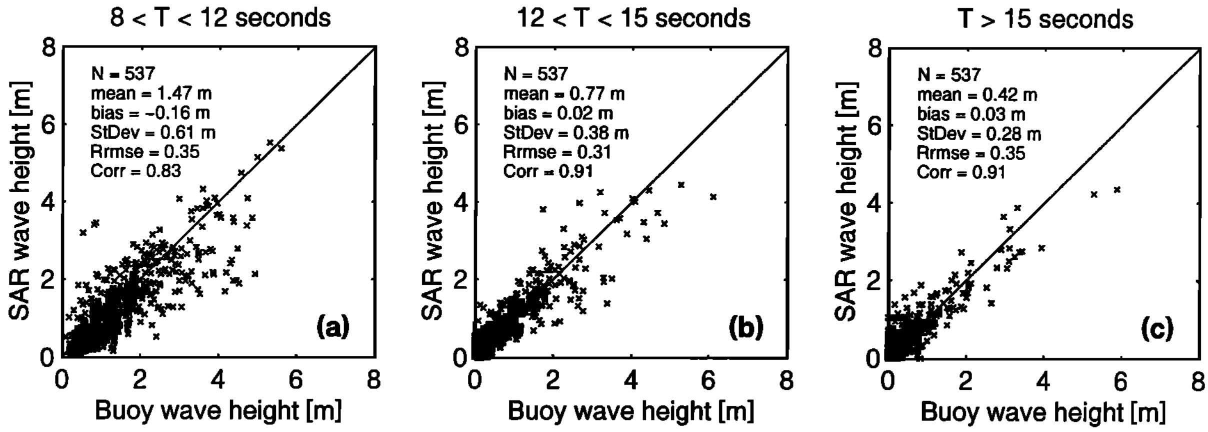

Figure 10. Retrieval of the height of the wave components in three different frequency intervals: (a) wave period between 8 and 12 s (length between 100 and 225 m), (b) wave period between 12 and 15 s (length between 225 and 350 m), and (c) waves with periods longer than 15 s (> 350 m in deep water).

where g is the gravitational acceleration. In Figure 11 this estimate, using only the wind speed from the scatterometer, is compared to the output of the SPRA inversion scheme, which uses both the SAR and the scatterometer data. It is clear that the H_s estimate benefits significantly from the SAR data: The standard deviation and the relative RMS error go down by 40%. The most important improvement comes from the SAR's ability to capture the swell. However, in a number of cases the wave height was reduced, which means that the SAR data indicated that the wind sea was not fully developed.

The above example shows that the SAR provides information on the sea state, additional to that which can be derived from the wind speed alone. Another question is, how much is the wave spectrum retrieval hampered by inaccuracies in the scatterometer wind estimate? To answer this question, the SPRA scheme has been applied with the wind observed by the buoy rather than by the scatterometer. The results of this run are summarized in Table 3. The validation results for the wave components with a period longer than 12 s show that errors in the scatterometer wind estimate do not contribute to the overall error made with the SPRA scheme.

In Figure 10 it is shown that the height of wave components longer than 12 s is retrieved with a negligible bias. This is consistent with the discussion in Appendix B, where it is shown that swell components longer than 140 m are not subject to the azimuthal blurring. Figure 11 indicates that the results obtained with the SPRA scheme have a negative bias of 0.30 m in the significant wave height. This is due to the fact that depending on the wind speed, there may be a spectral gap between the wind sea and the shortest wave resolved by the SAR. As no wave information is available in this region the energy density is set to zero. This causes the overall significant wave height to be underestimated.

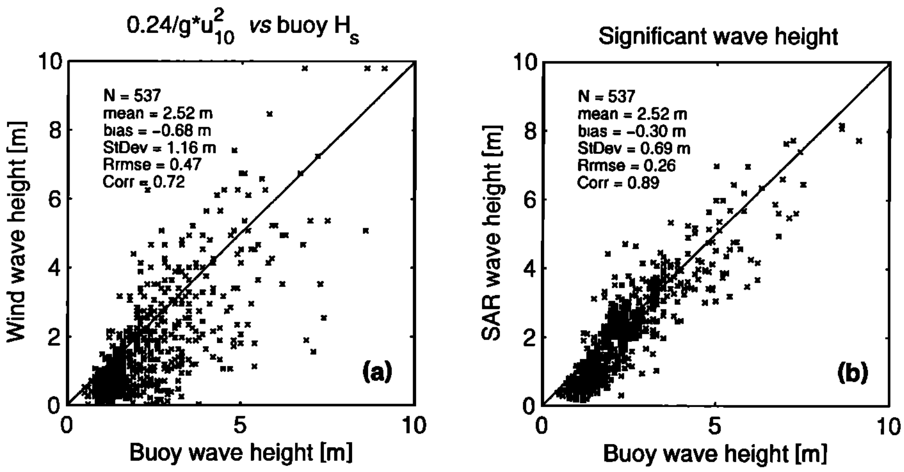

Figure 11. Retrieval of the significant wave height (a) from scatterometer only and (b) from combination of SAR and scatterometer.

Table 3. Comparison of the Statistics of Three Different Runs With the Semiparametric Retrieval Algorithm (SPRA): With the Standard Method, Using Buoy Rather Than Scatterometer Wind Measurements, and Without Wind-Dependent Tilt Modulation.

	Standard	Buoy Wind	Old Tilt
N	537	537	537
Bias, m	0.03	0.00	0.13
s.d., m	0.41	0.45	0.47
RRMSE	0.29	0.32	0.35

The Data Refers to the height of the wave components longer than 12 s.

Another integral parameter that can be calculated from the retrieved ocean wave spectrum is the mean wave period. For the present purpose a mean wave period T_m, defined as

$$T_m = \frac{\int f^{-1} F df}{\int F df}, \tag{12}$$

is used. Compared to the zero upcrossing period, which is mainly determined by the level of the short wind waves, T_m is more sensitive to the presence of long swell waves. In Figure 12 the wave period calculated from the retrieved wave spectra is plotted against the buoy wave period. We find that the periods of wave systems dominated by short waves are underestimated, and those dominated by long waves are overestimated. The reasons for this behavior and for the underestimation of the significant wave height are the same: the lack of data in the spectral gap between the wind sea and the shortest wave component resolved by the SAR in light to moderate wind conditions. Because on average spectral wave energy is missing in the middle of the spectrum, the SPRA method has a slight tendency to exaggerate the mean wave period.

3.5. Effect of a Wind-Dependent Tilt Modulation

The SPRA scheme uses a wind-dependent tilt modulation that is derived from the CMOD4 relation between the surface wind and the radar backscatter (see section 2.3). An alternative to this approach is to use a wind independent tilt modulation such as the one described by HH91. Figure 2 illustrates the difference between the two: For low wind speeds the amplitude of the tilt modulation is enhanced, for high wind speeds it becomes direction dependent. In this section we will assess the effect that the wind-dependent tilt modulation has on the retrieved wave heights.

In Table 3 the validation results of a run with and without the CMOD4-derived tilt are listed. Compared to the calculations with the tilt formulation from HH91, the scatter is reduced by more than 10%. This can be attributed in particular to a better performance in cases with a wind speed less than 10 m/s. Figure 13 shows a comparison of the retrieval of the height of the wave components longer than 12 s for three different wind speed ranges. Note that the performance of the retrieval in relative terms is reasonably constant at around 30% over the whole wind speed range.

In Table 4 the statistics for the runs with and without the CMOD4 tilt modulation are listed for the same three wind speed ranges. This table reveals that the largest reduction in scatter due to the wind dependence is achieved for wind speeds lower than 10 m/s. For wind speeds lower than 6 m/s the relative RMS is reduced from 37% to 27%, for wind speeds between 6 and 10 m/s it is reduced from 41% to 32%. The effect of the directional sensitivity of the tilt modulation, which was particularly pronounced for wind speeds over 10 m/s, is much smaller, but still positive (RRMSE from 31% to 29%).

3.6. Filtering Out Nonwave Features

In section 2.5 the algorithm is described that is used to clean the SAR image spectra from nonwave features. Here we evaluate the merits of this method by switching it off. In Figure 14 the retrieved height of waves longer than 225 m is compared with buoy data, both without filtering (Figure 14a) and with filtering (Figure 14b). It is clear that the performance of the retrieval algorithm benefits greatly from the elimination of nonwave features: the standard deviation decreases from 0.65 m to 0.42 m, and the bias is reduced from 0.18 m to less than a centimeter.

Note that of the 595 available SAR spectra, about 10% were rejected completely because of contamination by nonwave features. Other retrieval algorithms reject a far larger fraction of the available measurements: *He-*

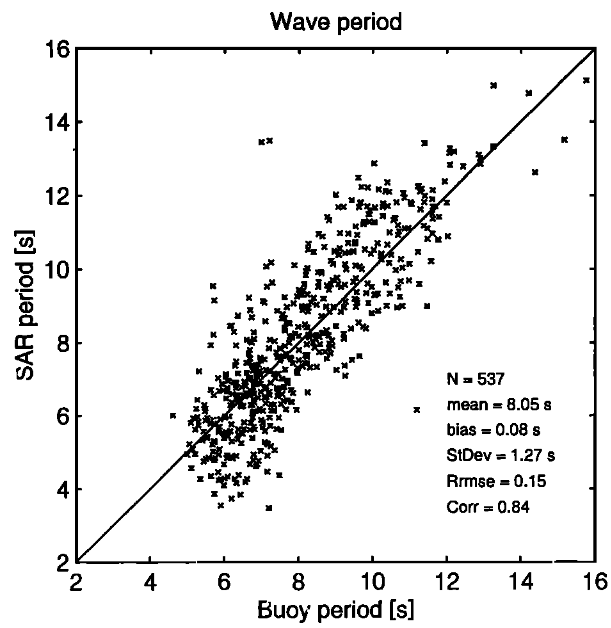

Figure 12. Comparison of the retrieved mean wave period with buoy measurements.

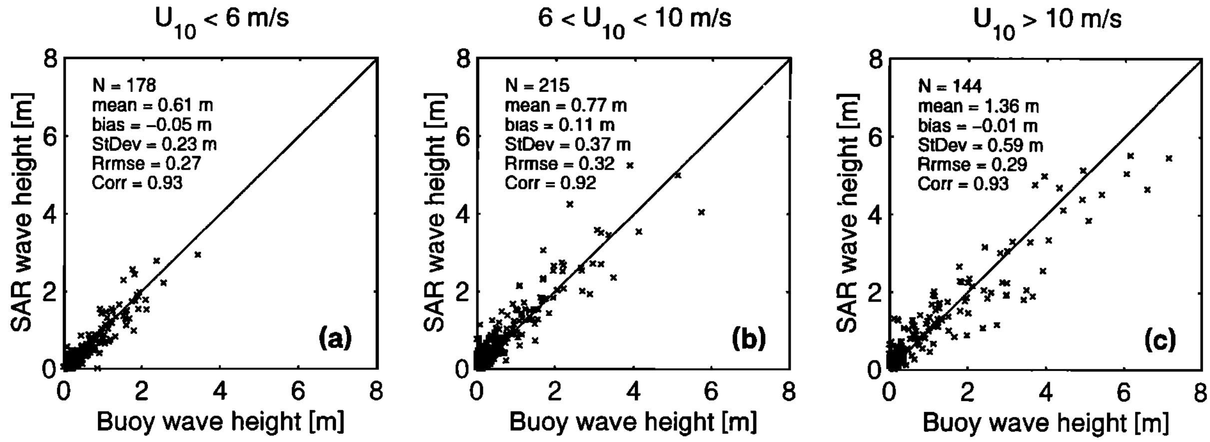

Figure 13. Retrieval of the height of the wave components longer than 12 s for different wind speed ranges: (a) $U_{10} < 6$ m/s, (b) $6 < U_{10} < 10$ m/s, and (c) $U_{10} > 10$ m/s.

imbach et al. [1998] reported a rejection percentage of 30%, *Breivik et al.* [1998] rejected half of the SAR observations. As we intend to use the data to assess the spectral wave climate, it is important that as large a fraction of the data as possible gets interpreted. Our filtering method accomplishes this by rejecting only the contaminated part of SAR spectra, rather than rejecting all contaminated observations.

4. Comparison With Directional Wave Buoy Measurements in the North Sea

The validation of the SAR wave mode retrieval algorithm in the previous section has been limited to the spectral distribution of the energy density. Three quarters of the wave buoys employed by NOAA only report a one-dimensional wave spectrum. With the exception of a single buoy near Hawaii, all the directional NOAA buoys are located close to the shore, in areas where the wave field can not be expected to be spatially homogeneous. Alternatives to the NOAA data set are scarce. The U.K. Meteorological Office operates a network of 10 buoys in the northeastern Atlantic that provides only two integral wave parameters: the significant wave height and the zero-crossing wave period. For the validation of the spectral capabilities of the SAR this is clearly insufficient.

A limited collocation could be made with direction wave data of two buoys deployed in the southern part of the North Sea. These buoys, located near the offshore platforms k13 and auk (Figure 15), report both the energy density and the propagation direction as a function of frequency at 3 hour intervals. Though several years of buoy data were available, the collocation rendered only a dozen cases. The reason for this low yield is that the ERS SAR is often switched in image mode in this region. Most of the cases which could be matched were not very interesting due to a lack of long waves. In Figures 16 to 19 two cases are analyzed: the first near auk (56°24'N, 2°4'E), and the second near k13 (53°13'N, 3°13'E). The directional information from the buoy is indicated as a thick, solid line in the two-dimensional plots of the retrieved wave spectrum (bottom right panels in Figures 16 and 18).

The first case (Figures 16 and 17) was acquired March 17, 1993. The scatterometer indicates that a wind of 12 m/s was blowing toward the satellite. The longest components of the wind waves are just visible on the SAR spectrum. More pronounced on the SAR spectrum is the swell system traveling in the azimuthal direction. The peak wavelength of this swell system is almost 500 m, which corresponds to a wave period of about 17 s in deep water. The water depth near auk is 80 m, which has a limited effect on the energy and

Table 4. Validation of the Retrieval of the Height of Wave Components Longer Than 12 s With and Without a Wind-Dependent Tilt Formulation For Three Different Wind Speed Ranges

	$U_{10} < 6$ m/s		$6 < U_{10} < 10$ m/s		$U_{10} > 10$ m/s	
	Standard	Old Tilt	Standard	Old Tilt	Standard	Old Tilt
N	178	178	215	215	144	144
Mean, m	0.61	0.61	0.77	0.77	1.36	1.36
Bias, m	-0.05	0.06	0.11	0.23	-0.01	0.08
s.d., m	0.23	0.31	0.37	0.44	0.59	0.63
RRMSE	0.27	0.37	0.32	0.41	0.29	0.31

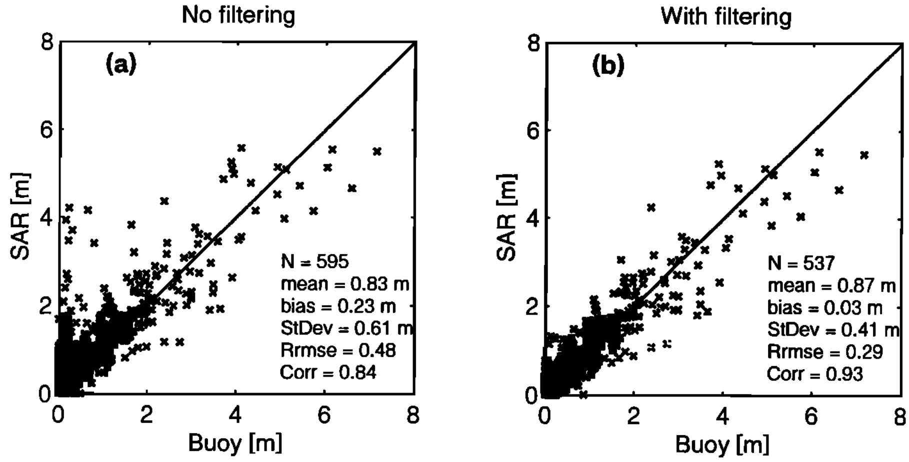

Figure 14. Retrieved height of wave components longer than 225 m (a) without and (b) with applying the routine that filters out nonwave features from the observed SAR spectrum.

period of the retrieved wave spectrum. The energy density spectra (Figure 17) show that this swell system has a very limited amplitude: Its height is less than 0.2 m. Nevertheless, both the energy distribution and the propagation direction are well picked up by the SAR. The thick line in the bottom right spectrum of Figure 16, which represents the wave direction measured by the buoy, shows that the swell system is propagating SSE. This is in perfect agreement with the wave spectrum derived from the SAR data, when keeping in mind that this spectrum has an 180° ambiguity in the swell propagation direction. As indicated by the solid line in the wave spectrum in Figure 16, the propagation direction of waves shorter than 150 m observed by the buoy coincides with the wind direction observed by the scatterometer (indicated by the arrow).

The second example was recorded on November 10, 1995 near platform k13. The depth in this part of the North Sea is only 25 m, shallow enough to affect the 180 m long swell visible on the SAR image in Figure 18. Again the swell has a limited amplitude, less than 0.2 m according to the buoy measurement. Nevertheless, both the energy distribution and the propagation direction derived from the SAR measurement are in good

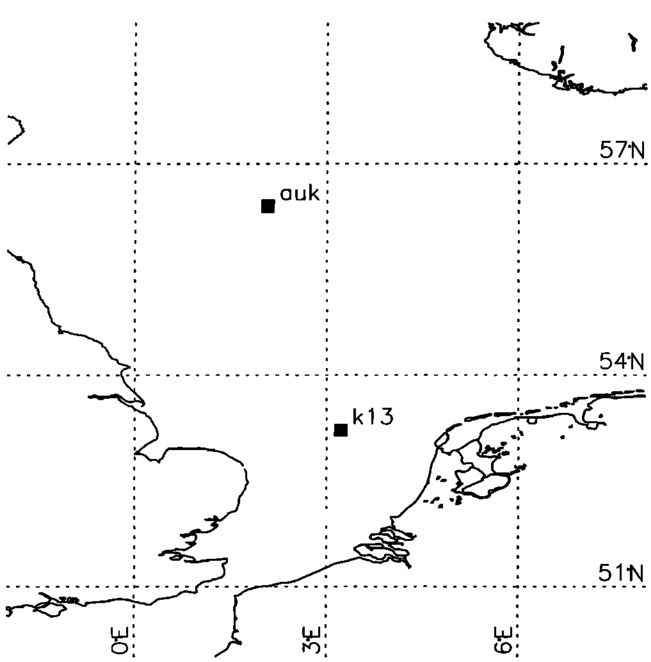

Figure 15. Locations of the directional wave buoys auk and k13 in the southern part of the North Sea.

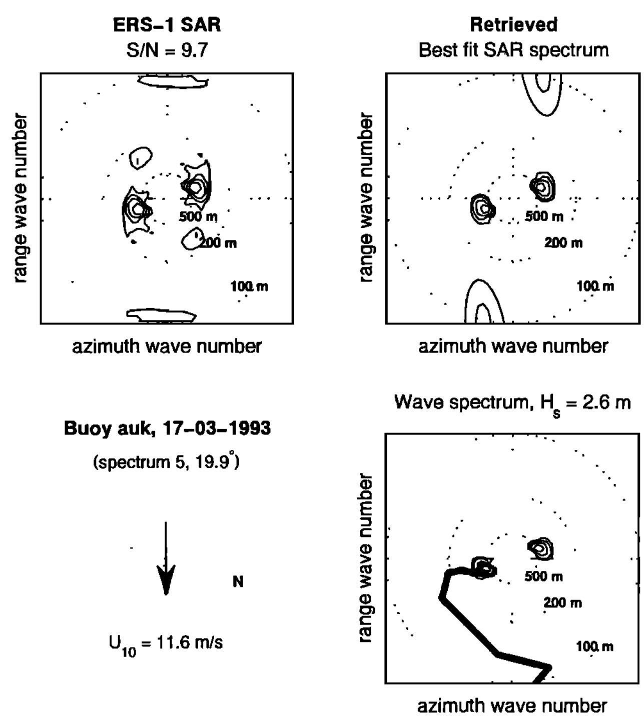

Figure 16. Example of a wave spectrum near auk with 500 m swell waves propagating to the south (March 17, 1993, 2148 UT). The thick, solid line in the bottom right spectrum indicates the propagation direction observed by the buoy.

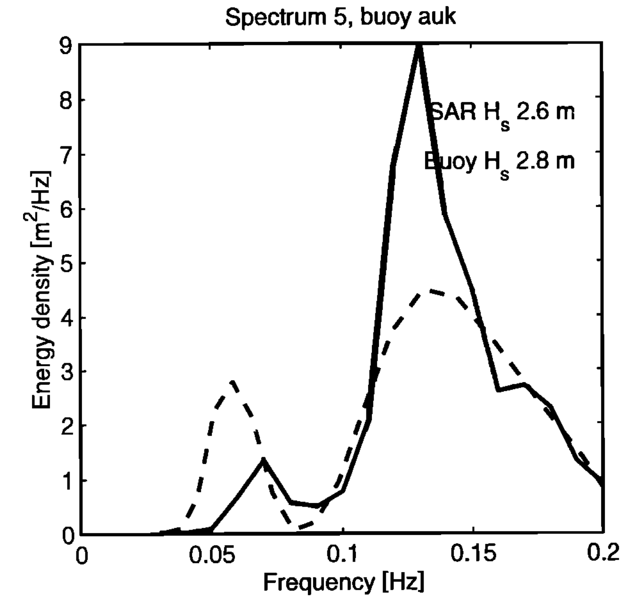

Figure 17. Observed and retrieved energy density spectra for the case in Figure 16. Solid line denotes buoy observation; dashed line denotes wave spectrum derived from SAR.

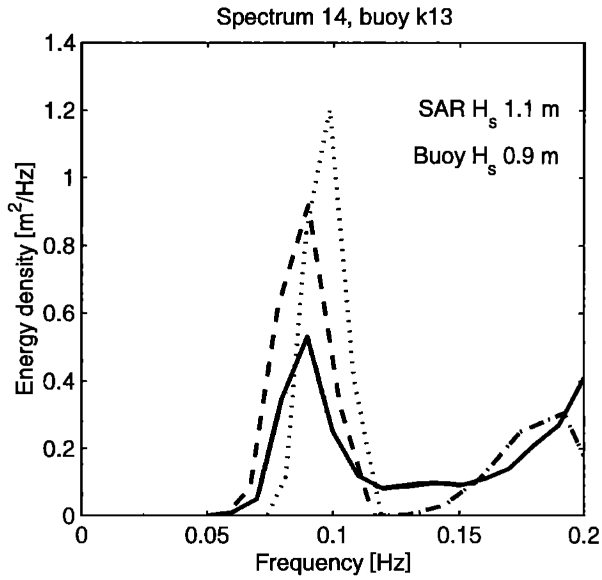

Figure 19. Effect of the limited depth (30 m) near k13: when an unlimited depth is assumed (dotted line), the frequency of the swell is overestimated compared to the buoy observations (solid line).

agreement with the in situ data. There is even an indication that the effect of the limited depth shows up when the spectra from the satellite and the buoy are compared. To convert the wave number spectrum that can be derived from the spatial SAR observation to the frequency spectrum from the temporal buoy measurement, we need the dispersion relation. When we use

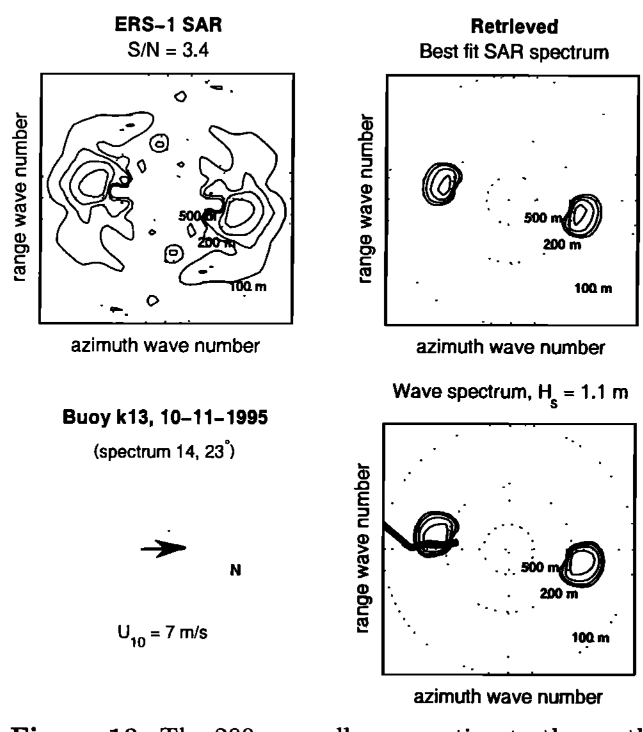

Figure 18. The 200-m swell propagating to the south near k13 (November 10, 1995, 2147 UT). The propagation direction observed by the buoy is indicated in the bottom right spectrum with a thick, solid line.

the dispersion relation for deep water for this purpose (dotted line in Figure 19), we find that the peak frequency of the swell is higher than the one observed by the buoy. When the limited depth is taken into account (dashed line), the peak frequencies match perfectly.

Though the number of directional cases that could be analyzed was limited, the above examples clearly illustrate the directional capability of the SAR data. In these examples the propagation direction could be found within 15°. To establish the directional accuracy with greater certainty, more validation will be necessary.

5. Comparison With the MPI Retrieval Algorithm

The retrieval algorithm described by HH91, which has been used and modified in several subsequent papers [*Brüning et al.*, 1994; *Hasselmann et al.*, 1996; *Heimbach et al.*, 1998], differs in several respect from the semiparametric algorithm described here. Both methods use the same nonlinear mapping relation, but they differ in the way this relation is inverted. To overcome the 180° ambiguity problem, the scheme developed at the Max Planck Institute (MPI) uses a first guess wave spectrum, usually obtained from a numerical model.

The present version of the MPI scheme, described by *Heimbach et al.* [1998], performs two nested iteration cycles. In the inner loop, the SAR spectrum is inverted on a discrete wave number grid by minimizing a cost function measuring the mismatch between the SAR spectrum and the first guess. It uses the HH91 model to predict the SAR spectrum, and the inverse of the quasi-linear approximation to map the prediction error back to an update of the ocean wave spectrum.

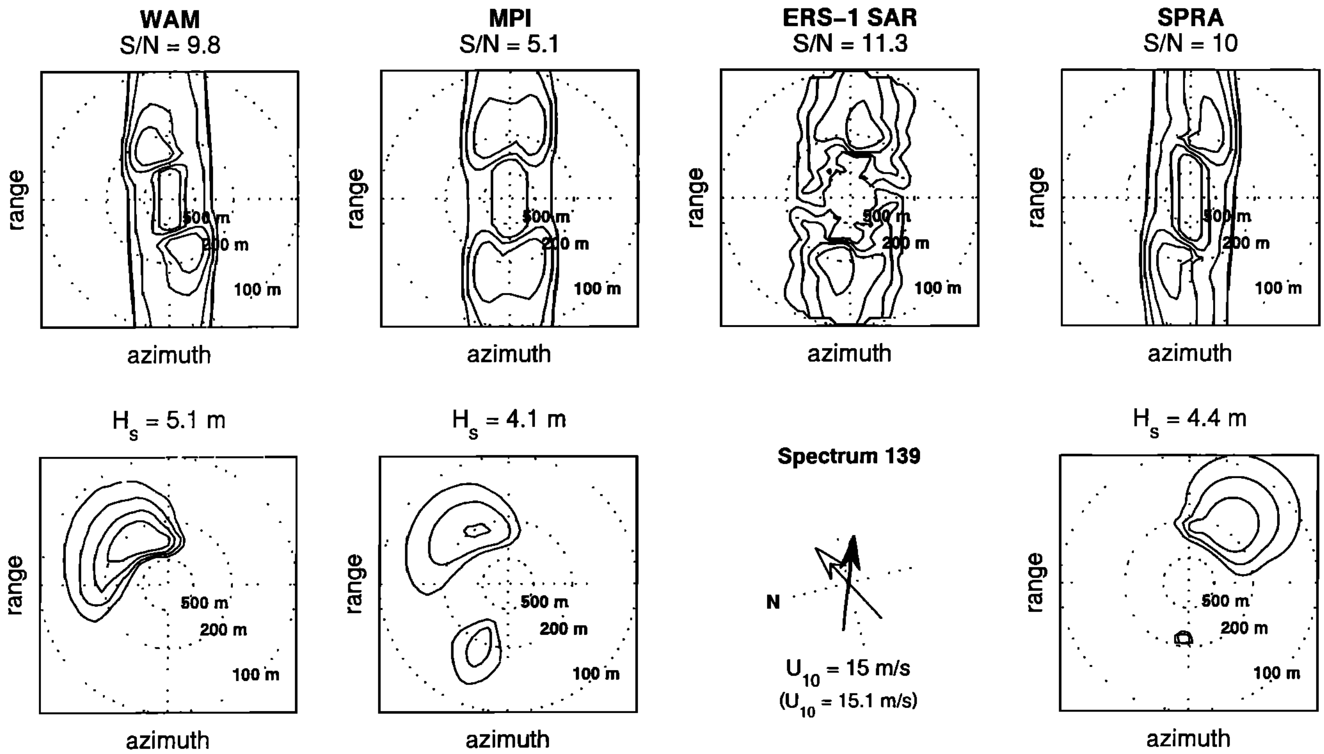

Figure 20. Comparison with the Max Planck Institute (MPI) scheme using an observation acquired south of Newfoundland (39°N, 57°W) on January 30, 1993 at 1434 UT. This case corresponds to figure 7 of *Hasselmann et al.* [1996]. Columns: first guess from the wave model WAM, spectra retrieved with MPI scheme, observed SAR spectrum and wind vector, and spectra retrieved with the SPRA scheme. The open tipped arrow corresponds to the European Centre for Medium Range Weather Forecast (ECMWF) model wind, and the solid tip arrow to the scatterometer wind.

Also the ocean wave spectrum is scaled to match an azimuthal cutoff value determined empirically from the observed SAR spectrum. In the outer loop the solution is matched by shifting and scaling of spectral partitions to generate a new first guess for the next inner iteration.

Both SAR retrieval algorithms have been compared for 142 spectra acquired by ERS-1 on January 30, 1993. No independent in situ data are available for these cases. Of the 142 measurements, 73% passed the quality control of the MPI inversion algorithm. This is consistent with the rejection percentage of 30% reported by *Heimbach et al.* [1998] for a 3 year global data set.

Though the wave heights retrieved by both schemes coincide to a certain degree, this is hardly the case for the underlying two-dimensional spectra. This is illustrated by the example shown in Figure 20, an example also used by *Hasselmann et al.* [1996] (their Figure 7). The wave spectrum retrieved with the MPI scheme as shown here differs in details from that in the work by *Hasselmann et al.* [1996] as for the results presented here, the latest available version of the MPI algorithm was used.

The observed SAR spectrum shows a clear peak, with a wavelength of 225 m. The SPRA scheme matches this peak with a slightly underdeveloped (U_{10}/c_p=1.2) wind sea, propagating in the wind direction as detected by the scatterometer. Given the consistency between the SAR spectrum and the observed wind, this solution seems very probable. The scatterometer wind direction (solid arrow in Figure 20) differs about 40° from the one in the meteorological model that was used to produce the wave model first guess (arrow with open tip). Note that the scatterometer wind direction coincides with the propagation direction of the wave system observed by the SAR. This fact is exploited by the SPRA algorithm, which is able to reproduce the observed SAR spectrum with a single wind sea spectrum, propagating at a small angle to the wind.

Starting from the first guess wave spectrum, the MPI scheme reduces the energy of the wave system propagating in the model wind direction. A second peak, propagating exactly against the wind observed by the scatterometer, is increased. This example illustrates two points. First, the dependence of the MPI retrieval on the wave model first guess goes beyond merely the elimination of the 180° ambiguity in the propagation direction of the waves. The fact that the first guess is the starting point of their iterative procedure is clearly reflected in the end result. Second, both schemes do not necessarily interpret a given SAR observation in the same way. In this particular example the angular distributions of the wave energy obtained from both inversion schemes are very different. This leads to the conclusion that a more comprehensive intercomparison, involving in situ measurements of the wave spectrum, is necessary to determine the merits of both schemes.

6. Summary and Conclusions

The SAR wave mode observations collected by the ERS-1/2 satellites since 1991 constitute the only set of spectral wave observations with a global coverage. In this paper a retrieval algorithm is presented that aims to extract spectral wave information from these SAR spectra in order to derive improved wave climate information. The method inverts the nonlinear mapping relations first described by *Hasselmann and Hasselmann* [1991] without using a priori information on the sea state. The wave spectrum is retrieved in two steps. Combining the scatterometer wind estimate with the observed SAR spectrum, the most likely wind sea parameters are estimated. The wind sea peak is parameterized using the spectral shape proposed by *Donelan et al.* [1985]. Given this wind sea spectrum, the swell peaks are determined from the residual signal in the observed SAR spectrum. The inversion algorithm, named the semiparametric retrieval algorithm (SPRA), has been validated by collocating 5 years of satellite data with 11 spectral NOAA buoys. Also, limited comparisons have been made with two directional buoys in the North Sea, and with output from the retrieval algorithm of *Hasselmann and Hasselmann* [1991]. This has led to the following conclusions:

1. In the interpretation of spaceborne SAR data, the nonlinear character of the relations that map an ocean wave spectrum onto a SAR image spectrum should be faithfully represented. The relatively steep wind waves associated with moderate to strong winds cause low azimuth wave number ridges in the SAR image spectrum. A retrieval algorithm can benefit from these features as they contain information on wave systems that may be otherwise invisible to the SAR. The low azimuth wave number ridges caused by wind waves can be misleading when they are interpreted as long swell waves, which happens when the quasi-linear model is used in the inversion.

2. A wind-dependent formulation for the tilt modulation has been derived from the empirical CMOD4 relation, as an alternative to the wind-independent tilt modulation used in HH91. The new tilt reduces the scatter in retrieved wave heights significantly, in particular for cases when the wind speed is below 10 m/s.

3. Overall, the SPRA method is capable of retrieving the height of wave components longer than 225 m with an accuracy of 0.40 m, which corresponds to a relative error of 30%. The retrieval of integrated spectral parameters such as the significant wave height or the mean period is somewhat biased by the absence of information on waves longer than the wind sea, but shorter than those explicitly resolved by the SAR.

4. An essential part of the SPRA algorithm is the screening of observed SAR spectra for nonwave features, and the removal of these features. The present filtering routine exploits the fact that spectra contaminated by slicks seem to have a spectral signature that is distinctly different from that caused by ocean waves. Only about 10% of the spectra are completely rejected; in the majority of cases only the longest few wavelengths are filtered out.

5. A comparison with a limited set of directional buoy measurements indicates that the angular results obtained with the SAR are quite accurate, and may be of the same order as the grid spacing of the SAR wave mode product itself (15°).

6. Finally, a preliminary comparison with results from the retrieval algorithm from HH91 reveals quite substantial differences. These differences, which are most apparent in the two-dimensional distribution of wave energy, can be well explained given the different strategies employed by both schemes. A more comprehensive intercomparison, which includes independent in situ data, will be necessary to evaluate the relative strengths of both methods.

The SPRA scheme has been applied to all SAR wave mode observations acquired since 1991. The resulting ocean wave spectra are being used to provide spectral wave climate data to the offshore industry.

Appendix A: Derivation of the Cost Function

In the retrieval algorithm the difference between an observed and a simulated SAR spectrum is expressed in terms of a cost function. The functional form of this cost function is derived from the statistics obeyed by the coefficients making up a SAR spectrum. The complex Fourier coefficient a_{obs} of a SAR image in a particular wave number is approximately Gaussian with independent real and imaginary parts [*Brillinger*, 1975], so its probability density is

$$f(a_{obs}) = (\pi s)^{-1} \exp(-|a_{obs}|^2/s), \qquad \text{(A1)}$$

where $s = \langle |a_{obs}|^2 \rangle$ is the variance of the complex Fourier amplitude. Here s is by definition directly proportional to the SAR spectral density. Let a_{obs} be scaled such that s is the SAR spectral density. Assuming that Fourier coefficients at different wave numbers are independent (an approximation which strictly holds only if the image is Gaussian), the joint density of m Fourier coefficients at the same wave number (or at neighboring wave numbers, assuming a locally homogeneous spectral density) is a product of (A1):

$$f(a^1_{obs}, ..., a^m_{obs}) = (\pi s)^{-m} \exp(-m s_{obs}/s), \qquad \text{(A2)}$$

with

$$s_{obs} = \frac{1}{m} \sum_{i=1}^{m} |a^i_{obs}|^2 \qquad \text{(A3)}$$

the mean square value of the Fourier coefficients, which is also the estimate of the SAR spectrum. Our model, that is, the forward mapping of HH91 combined with a parameterized wind sea spectrum, supposedly describes the SAR spectral density s. We therefore choose the free parameters in that model, the wave age and mean propagation direction, such that the observed Fourier coefficients are most likely, or in other words, such that their probability density (A2) given the SAR spectrum s is maximal. From (A2), we see that this is equivalent to minimizing

$$J = -\log f(a^1_{obs}, ..., a^m_{obs}) = m \log s + \frac{m s_{obs}}{s} + m \log \pi. \tag{A4}$$

Equation (A4) gives the contribution to the cost associated with a single spectral bin. Assuming independence of Fourier coefficients in different bins, the overall cost is obtained by summing terms (A4) over all wave number bins. As we carry out the summation over a square Cartesian wave number grid, the "degrees of freedom" m are the same in all bins so they are irrelevant to the solution. Usually a cost function is used that is quadratic in the difference between the modeled value s and the observed value s_{obs} [e.g., *Hasselmann et al.*, 1996]. This form can be obtained from (A4) by making an expansion around the minimum $s = s_{obs}$. Compared to the quadratic form, the present cost function penalizes values smaller than the observation, and favors larger values.

Appendix B: Nonlinearity SAR Mapping Relations

The nonlinearity of the SAR mapping relations depends on the dimensionless azimuth wave number $\kappa = k_x \beta \langle v^2 \rangle^{1/2}$, where β is the slant range divided by the SAR platform velocity and $\langle v^2 \rangle$ is the variance of the orbital velocity component in the slant range direction. Short azimuth wave components, with $\kappa \gg 1$, are not visible to the SAR, as nonlinear effects degrade the azimuth resolution. For long azimuth wave components, with $\kappa \ll 1$, the mapping relations are linear. By using some simple scaling arguments, it is possible to estimate which part of a wave spectrum can be expected to be obscured by nonlinear effects, and which part of the spectrum is mapped linearly.

As the orbital velocity variance depends on a higher moment of the wave spectrum, the main contribution to the orbital velocity variance comes from the shorter wind waves rather than from the longer swell waves. Using standard, empirical relations for the spectral shape of the wind sea spectrum, the orbital velocity variance can be expressed in terms of the peak wave number of the wind sea. In first approximation the orbital velocity variance is inversely proportional to the wind sea peak wave number k_p:

$$\langle v^2 \rangle = \alpha \frac{g}{k_p}, \tag{B1}$$

where α is the (dimensionless) Phillips constant, and g is the gravitational acceleration. Using this empirical relation, the dimensionless azimuth wave number can now be written as:

$$\kappa = \frac{k_x}{(k_p k_{SAR})^{1/2}}, \tag{B2}$$

where k_{SAR} is a fixed wave number that is determined by a property of the measuring device, and by physical constants governing wind sea spectra:

$$k_{SAR} = \frac{1}{\beta (\alpha g)^{1/2}}. \tag{B3}$$

With a Phillips constant $\alpha \simeq 4 \times 10^{-3}$, and $\beta \simeq 110$ s for the ERS-1/2 SAR, it follows that $k_{SAR} = 0.045$ rad/m, which corresponds to a wavelength of 140 m.

The above scaling argument shows that in first approximation, the cutoff wave number does not depend only on the level of the wind sea waves. A combination of physical constants governing the spectral level and shape of wind spectra (α and g) and a physical property of the measuring device (β) introduce a second length scale. For the ERS-1/2 SAR this length scale happens to be 140 m, which is inside the spectral range of ocean waves that we hope to detect with the SAR. This means that the SAR will never resolve azimuth-traveling wind sea waves which have a peak wavelength shorter than 140 m, independent of the spatial resolution of the SAR. On the other hand, the longest wave components of an azimuth-traveling wind sea spectrum with a peak longer than 140 m will be visible. It also follows that swell waves, which may be assumed to be longer than the wind sea waves, are mapped linearly in the relevant spectral domain between 100 and 1000 m. Note that this argument rests on the fact that the intrinsic length scale of 140 m is close to the lower boundary of our present spectral range. If the spectral range of the SAR wave mode product were to start at 20 m, such as foreseen for the ENVISAT mission, some azimuth-traveling swell components falling in this spectral range will actually get blurred. In other words, the shortest spectral bins in the azimuth direction will not contain wave information, no matter how light the wind conditions are.

Acknowledgments. Without the data from the buoy network operated by NOAA and disseminated by the NODC and the NBDC the present study would not have been possible. The two-dimensional wave spectra of the two buoys in the North Sea have been provided by Bram Roskam of RIKZ in the Netherlands. The authors wish to thank Susanne Hasselmann of the Max Planck Institute in Hamburg for supplying the data set with results from the MPI retrieval algorithm. This work is part of the COASTMON project (contract ENV4-CT96-0360) of the Centre for Earth Observation (CEO) programme, and has been financially supported by the Netherlands Remote Sensing Board BCRS under the contracts 1.1/AP-02 and 1.1/AP-06.

References

Alpers, W., and K. Hasselmann, Spectral signal to clutter and thermal noise properties of ocean wave imaging synthetic aperture radars, *Int. J. Remote Sensing*, *3*, 423-446, 1982.

Apel, J.R., An improved model of the ocean wave vector spectrum and its effects on radar backscatter, *J. Geophys. Res.*, *99*, 16,269-16,291, 1994.

Breivik, L.A., M. Reistad, H. Schyberg, J. Sunde, H.E. Krogstad, and H. Johnsen, Assimilation of ERS SAR wave spectra in an operational wave model, *J. Geophys. Res.*, *103*, 7887-7900, 1998.

Brillinger, D.R., *Time Series - Data Analysis and Theory*, 500 pp., Holt, Rinehart, and Winston, Austin, Tex., 1975.

Brüning, C., S. Hasselmann, K. Hasselmann, S. Lehner, and T. Gerling, A first evaluation of ERS-1 synthetic aperture radar wave mode data, *Global Atmos. Ocean Syst.*, *2*, 61-98, 1994.

Donelan, M.A., J. Hamilton, and W.H. Hui, Directional spectra of wind generated waves, *Philos. Trans. R. Soc. London*, *315*, 509-562, 1985.

Engen, G., and H. Johnsen, SAR-ocean wave inversion using image cross spectra, *IEEE Trans. Geosci. Remote Sens.*, *33*, 1047-1056, 1995.

Garello, R., and J.M. Le Caillec, SAR imaging of the ocean surface: Nonlinearities simulation and estimation, *Paper presented at* 1997 International Geoscience and Remote Sensing Symposium, 1997.

Hasselmann, K., and S. Hasselmann, On the nonlinear mapping of an ocean wave spectrum into a synthetic aperture radar image spectrum and its inversion, *J. Geophys. Res.*, *96*, 10,713-10,729, 1991.

Hasselmann, K. et al., Measurement of wind-wave growth and swell decay during the Joint North Sea Wave Project (JONSWAP), *Dtsch. Hydrogr. Z. Suppl. A*, *8*, 95 pp., 1973.

Hasselmann, K. et al., Theory of synthetic aperture radar ocean imaging: A MARSEN view, *J. Geophys. Res.*, *90*, 4659-4686, 1985.

Hasselmann, S., C. Brüning, K. Hasselmann, and P. Heimbach, An improved algorithm for the retrieval of ocean wave spectra from synthetic aperture radar image spectra, *J. Geophys. Res.*, *101*, 16,615-16,629, 1996.

Heimbach, P., S. Hasselmann, and K. Hasselmann, Statistical analysis and intercomparison of WAM model data with global ERS-1 SAR wave mode spectral retrievals over 3 years, *J. Geophys. Res.*, *103*, 7931-7977, 1998.

Keller, W.C., and J.W. Wright, Microwave scattering and straining of the wind generated waves, *Radio Sci.*, *10*, 139-147, 1975.

Kerbaol, V., B. Chapron, and P.W. Vachon, Analysis of ERS-1/2 synthetic aperture radar wave mode imagettes, *J. Geophys. Res.*, *103*, 7833-7846, 1998.

Krogstad, H.E., A simple derivation of Hasselmann's nonlinear ocean-synthetic aperture radar transform, *J. Geophys. Res.*, *97*, 2421-2425, 1992.

Krogstad, H.E., O. Samset, and P.W. Vachon, Generalizations of the nonlinear ocean-SAR transform and a simplified SAR inversion algorithm, *Atmos. Ocean*, *32*, 61-82, 1994.

Laur, H., P. Bally, P. Meadows, J. Sanches, B. Schättler, and E. Lopinto, ERS SAR calibration: Derivation of the backscattering coefficient σ_0 in ESA ERS SAR PRI products, ESA doc. ES-TN-RS-PM-HL09, Eur. Space Res. and Technol. Cent., Noordwijk, Netherlands, 1996.

Le Caillec, J.M, R. Garello, and B. Chapron, Two dimensional bispectral estimates from ocean SAR images, *Nonlinear Processes Geophys.*, *3*, 196-215, 1996.

Long, R.B., The statistical evaluation of directional spectrum estimates derived from pitch/roll buoy data, *J. Phys. Oceanogr.*, *10*, 944-952, 1980.

Quilfen, Y., and A. Bentamy, Calibration/validation of ERS-1 scatterometer precision products, in: *ERS-1 Off-line wind scatterometer products*, edited by Y. Quilfen, 41-43, Inst. Fr. de Rech. Pour l'Exploitation de la Mer, Brest, 1995.

Stoffelen, A., and D. Anderson, Scatterometer data interpretation: estimation and validation of the transfer function CMOD4, *J. Geophys. Res.*, *102*, 5767-5780, 1997.

C. F. de Valk and C. Mastenbroek, ARGOSS, P.O. Box 61, 8325 ZH Vollenhove, Netherlands. (e-mail: valk@argoss.nl; kees@argoss.nl)

(Received September 2, 1998; revised July 29, 1999; accepted September 20, 1999.)